



Fast-moving Mesh Method and Its Application to Circumferential Non-uniform Tip Clearance in a Single-stage Turbine

Y. Zheng, X. B. Jin and H. Yang[†]

School of Energy and Power Engineering, Beihang University, Beijing 100191, China

†Corresponding Author Email: huiyang@buaa.edu.cn

ABSTRACT

The circumferential non-uniform tip clearance (CNTC) due to casing out-of-roundness adversely affects the turbine aerodynamic performance due to machining and assembly errors, thermal deformation, and improper active clearance control (ACC), etc. Moreover, the asymmetric computational domain caused by casing out-of-roundness presents difficulties for conventional numerical techniques that consider rotational periodicity. Since previous traditional methods using split computational domains have the disadvantages of high interpolation error and high time cost, an efficient fast-moving mesh (FMM) method based on an algebraic approach is proposed in this paper. This method is first validated by using a single-stage turbine with elliptical casing. The results show that the FMM has the advantages of high accuracy, high efficiency, and easy operation, which helps to solve the CNTC problem quickly in scientific research or engineering applications. Then, the effects of CNTC induced by the elliptical casing on the flow field and aerodynamic performance are investigated by using an in-house code that integrates the FMM method. Finally, the effect of stator row interference on the aerodynamic performance in the turbine stage with an elliptical casing is demonstrated. The results show that different types of elliptical casings have a significant effect on the aerodynamic performance. However, the variation law is not consistent (decreasing by 0.538% or increasing by 0.212%). Importantly, the novel finding of this paper is that this discrepancy is jointly determined by the interaction of multiple secondary flows (passage vortex, scraping vortex, etc.) at different spans, not just related to the variation of the tip leakage vortex (TLV) with tip size. Furthermore, this study is the first to indicate that the stator row interference can mitigate the extent of performance degradation due to elliptical casings by suppressing the development of secondary flows. These results may provide theoretical support for blade tip gap design and can also serve as a reasonable reference for the effective application of ACC in engineering. Finally, low-order harmonic components with high amplitudes are also innovatively found in the rotor row with a CNTC. These components may cause low-engine-order (LEO) resonances that endanger the safe operation of engines.

Article History

Received October 11, 2023

Revised February 17, 2024

Accepted February 20, 2024

Available online May 29, 2024

Keywords:

Circumferential Non-uniform Tip Clearance (CNTC)

Fast-moving mesh (FMM)

Elliptical casing

Interaction of multiple secondary flows

Stator row interference

1. INTRODUCTION

The tip clearance of an aero-engine turbine is one of the main factors affecting stage efficiency, with the ratio between turbine stage efficiency and tip size varying from 1:1 to 2:1 (Bunker, 2006). The tip clearance size usually changes during flight cycles and throughout an engine's lifetime due to machining and assembly errors, centrifugal loads, aerodynamic loads, and thermal loads (Olsson & Martin, 1982; Benito et al., 2008). Engine engineers have

attempted to mitigate the negative effects of excessive tip sizes through active clearance control (ACC) (Lattime & Steinetz, 2004; Lavagnoli et al., 2017). Although ACC limits variations in the tip size range by suppressing the thermal deformation of the casing, it aggravates the circumferential non-uniform deformation of the casing (Gaffin, 1979; hu et al., 2018), where the difference between the maximum and minimum thermal deformations can reach 0.3-0.91 mm. The circumferential non-uniform tip clearance (CNTC) caused by the casing out-of-roundness is one of the major factors that must be

NOMENCLATURE			
ΔS	entropy variation (dimensionless)	η	aerodynamic efficiency
A_{rate}	attenuation rate	A_{region}	influence region
ACC	active clearance control	C_{Ave}	average tip clearance
C_{Max}	maximum tip clearance	C_{Min}	minimum tip clearance
CFD	computational fluid dynamics	$CNTC$	circumferential non-uniform tip clearance
CPV	casing passage vortex	FMM	fast-moving mesh
$h_{t\ is\ out}$	outlet isentropic total enthalpy	$h_{t\ out}$	outlet total enthalpy
HE_*	high-loss regions	$HGAE$	hybrid grid aeroelasticity environment
LEO	low-engine-order	RBF	radial basis function
SST	shear stress transport	SV	scraping vortex
TFI	transfinite interpolation	TLV	tip leakage vortex
WV	wall vortex	y^+	non-dimensional wall distance

considered when designing turbine blade tips (Bunker, 2006; Liu et al., 2018).

In previous studies, the effects of CNTCs on rotor dynamic instabilities have been assessed (Alford, 1965; Song & Martinez-Sanchez, 1997a, b; Song, 1998; Pan et al., 2020); however, only a small proportion of previous related research has focused on the effects of CNTCs on turbine aerodynamic performance. Zheng et al. (2020) investigated the effect of CNTCs on the flow field and aerodynamic performance due to an elliptical casing employing an in-house code and showed that CNTCs significantly reduce the aerodynamic efficiency of the turbine stage (0.58%). The effect of CNTCs due to rotor-casing eccentricity on turbine efficiency was experimentally evaluated by DeShong et al. (2022). The results showed that the increase in efficiency in the small tip size region was balanced by the decrease in efficiency in the large tip size region and that the aerodynamic efficiency was not affected by the CNTC. The results of previous studies on the effect of CNTCs on the aerodynamic efficiency of turbine stages have been inconsistent. To accurately assess the impact of CNTCs on aerodynamic performance for engineering applications, resolving this contradiction is critical. It is thus indispensable to reveal the physical mechanism affecting aerodynamic efficiency in turbine stages with CNTCs from the flow field. Zheng et al. (2020) reported that the flow loss at different circumferential positions may be related to the tip leakage vortex scale. However, leakage vortices are not the only flow feature at the tip of the turbine blade. The interaction between several secondary flows, such as passage vortices and scraping vortices, is the main flow characteristic in this region. Additionally, stator row disturbances (wake, potential field, etc.) affect the development of secondary flows in the rotor row. Currently, it is unclear whether the effect of CNTCs on the efficiency of the turbine stage is related to the interactions between multiple secondary flows and stator-rotor interference. This makes it difficult to design and adapt appropriate control measures (e.g., ACC) to suppress the negative effects of CNTCs in engineering. Breaking the limitations in the understanding of the influence mechanism in previous studies is the focus of this study, which will provide a reasonable reference for determining tip sizes for the effective application of ACC in engineering fields. Moreover, this study can be used to

better help the turbine stage maintain high-performance operation.

For asymmetric computational domains due to elliptic casings, etc., regular numerical techniques that consider rotational periodicity cannot be performed (Chen et al., 2015, 2018; Jiang et al., 2020). The calculation domain is generally divided into an inner domain and an outer domain independently, in which the inner domain rotates and is axisymmetric, while the outer domain (including an elliptical casing) is stationary and non-axisymmetric. These two domains share a cylinder-shaped radial interface. The relative positions of the grids on either side of the interface change with time, and the flow profiles are interpolated across the interface, which may cause interpolation errors. Moreover, to facilitate data transmission on the cylinder-shaped radial interface, a small uniform blade tip clearance is set in the inner part, which also limits the minimum tip size that can be investigated via numerical simulations. In addition, for the numerical simulation of several layouts of elliptical casings and multi-blade rows, the geometric model, and the time cost increase significantly. Therefore, developing a new efficient method to address the shortcomings of traditional partitioned methods is important. Given the ongoing advances in numerical methods (with the rapid development of computational power), additional mesh generation techniques, which include two main methods, mesh reconstruction and mesh deformation, are effective at solving the above problem (Zhang, 2010). Compared with mesh reconstruction, mesh deformation does not change the topological connection between the original mesh points. Thus, new discrete calculation errors are not introduced, and the impact of geometric boundary changes on the flow field is more accurately distinguished. Therefore, mesh deformation is more widely used in engineering design. From the perspective of mesh implementation, the existing mesh deformation technologies can be divided into pseudo-structural approaches, partial differential equation methods, and algebraic methods. The algebraic methods, such as the transfinite interpolation (TFI) and radial basis function (RBF) methods (Gaitonde & Fiddes, 1993), which have not only good deformation mesh quality but also excellent mesh generation efficiency, are widely used in blade aeroelastic calculations (Allen, 2002; Zheng et al., 2012) and aerodynamic optimization of blade profiles (Reuther et al., 1996).

A new efficient method called the fast-moving mesh (FMM) method is proposed in this paper. This method can overcome the shortcomings of the traditional partitioned method for elliptical casings. Moreover, the FMM is integrated into the in-house Hybrid Grid Aeroelasticity Environment (HGAE) and used to perform further unsteady numerical studies. The accuracy of the FMM is first confirmed by a verification case on a single-stage turbine. To understand the effect of stator row interference on the aerodynamic performance of turbine stages with CNTCs, full-annulus unsteady aerodynamic simulations are conducted with only the rotor row and only the turbine stage. Then, the effect of CNTCs on the flow field and aerodynamic performance is analysed by comparing the flow field at the tip clearance and rotor exit for the different CNTC cases. Finally, the influence mechanism of CNTCs on the stage aerodynamic performance changes is determined from a flow physics perspective.

2. MODEL AND METHODS

2.1 Geometric Model

The geometrical model is the transonic turbine stage with published geometrical data from the Institute for Thermal Turbomachinery and Machine Dynamics. The meridional section of the turbine stage is shown in Fig. 1. The hub diameters of the stator and rotor rows are equal and, together with the casing contour, form a convergent-divergent meridional flow path. The main geometric characteristics are shown in Table 1. More detailed parameters can be found in the literature (Erhard & Gehrler, 2000; Göttlich et al., 2004). In this paper, the flat tip of the geometric model is used.

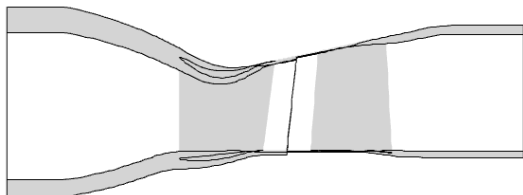


Fig. 1 Meridional section of turbine stage

Table 1 Geometric parameters

Parameter	Stator Row	Rotor Row
Airfoil count	24	36
Axial chord (midspan) (mm)	56.1	46.8
Pitch (mm)	60	41.6
Geometric turning angle (deg)	70	106
Airfoil height (mm)	55.2	69.8
Aspect ratio (exit height/chord)	0.70	1.25
Rotor tip clearance/span [%]	/	1.4
Pressure ratio (total to static)	3.50	
Rotational speed (rpm)	11000	
Reynolds number (exit)	2.57*10 ⁶	1.69*10 ⁶
Exit Mach number	1.11	0.46
Loading factor $\Delta h/u^2$	1.51	

2.2 Numerical Methodology

The procedure of the computational fluid dynamics (CFD) solver used to simulate the flow field of the turbine is HGAE, which is a three-dimensional, unsteady, time-accurate, Reynolds-Averaged Navier–Stokes (RANS) solver. The details and verification cases of the aerodynamic aspects of HGAE can be found in the published literature (Zheng (2004, Zheng & Yang, 2011, 2013; Zheng et al., 2022).

The integral form of the unsteady compressible Navier–Stokes equation is expressed as follows:

$$\frac{\partial}{\partial t} \int_{\Omega} \vec{U} d\Omega + \oint_{\partial\Omega} (\vec{F}_c - \vec{F}_v) dA = \int_{\Omega} \vec{H} d\Omega \quad (1)$$

where Ω is the control volume, $\partial\Omega$ is its boundary and dA represents the surface area of an element. \vec{U} represents the vector of conservative variables, \vec{H} is the source term vector, and \vec{F}_c and \vec{F}_v are the convective and viscous flux vectors, respectively.

The finite volume method is used to discretize the governing equations for multi-block grids. Roe’s approximate Riemann solver and the Monotone Upwind Scheme for Conservation Law extrapolation are implemented to calculate convective terms and central differences for the diffusion fluxes (Roe, 1981). The unsteady flow computations are conducted using Jameson’s dual time-stepping method for an implicit scheme with 15 sub-iterations (Jameson, 1991). The well-proven Menter Shear Stress Transport (SST) Turbulence Model is used for the calculation. More details can be found in Menter (1993, 1994).

2.3 Fast-Moving Mesh Method

When a CNTC is present, the rotor blades experience tip clearances of varying sizes as they rotate along the circumference. In turn, this process produces a computational domain that is unsteady and non-cyclic periodic, which violates the periodicity assumption inherent in the general approach. The drawbacks of the traditional partitioned method are described in the introduction. Thus, the fast-moving mesh method is proposed to effectively address this problem. It is a mesh deformation technique based on two algebraic approaches: transfinite interpolation (TFI) (Gaitonde & Fiddes, 1995) and radial basis function (RBF) interpolation (De Boer et al., 2007).

For TFI, the x-direction deformation at any point (i, j, k) in the internal field can be written as follows:

$$\Delta x_{i,j,k} = D_{\alpha}(x) + D_{\beta}(x) + D_{\gamma}(x) - D_{\alpha,\beta}(x) - D_{\beta,\gamma}(x) - D_{\alpha,\gamma}(x) + D_{\alpha,\beta,\gamma}(x) \quad (2)$$

where $D_{\alpha}(x)$, $D_{\beta}(x)$, $D_{\gamma}(x)$ are represented, respectively, as follows:

$$D_{\alpha}(x) = (1 - \alpha) \cdot \Delta x_{1,j,k} + \alpha \cdot \Delta x_{imax,j,k} \quad (3)$$

$$D_{\beta}(x) = (1 - \beta) \cdot \Delta x_{i,1,k} + \beta \cdot \Delta x_{i,jmax,k} \quad (4)$$

$$D_{\gamma}(x) = (1 - \gamma) \cdot \Delta x_{i,j,1} + \gamma \cdot \Delta x_{i,j,kmax} \quad (5)$$

Moreover, $D_{\alpha,\beta}(x)$, $D_{\beta,\gamma}(x)$, $D_{\alpha,\gamma}(x)$ and $D_{\alpha,\beta,\gamma}(x)$ are expressed as follows:

$$D_{\alpha,\beta}(x) = (1 - \alpha) \cdot (1 - \beta) \cdot \Delta x_{1,1,k} + \alpha \cdot (1 - \beta) \cdot \Delta x_{imax,1,k} + (1 - \alpha) \cdot \beta \cdot \Delta x_{1,jmax,k} + \alpha \cdot \beta \cdot \Delta x_{imax,jmax,k} \quad (6)$$

$$D_{\beta,\gamma}(x) = (1 - \beta) \cdot (1 - \gamma) \cdot \Delta x_{i,1,1} + \beta \cdot (1 - \gamma) \cdot \Delta x_{i,jmax,1} + (1 - \beta) \cdot \gamma \cdot \Delta x_{i,1,kmax} + \beta \cdot \gamma \cdot \Delta x_{i,jmax,kmax} \quad (7)$$

$$D_{\alpha,\gamma}(x) = (1 - \alpha) \cdot (1 - \gamma) \cdot \Delta x_{1,j,1} + \alpha \cdot (1 - \gamma) \cdot \Delta x_{imax,j,1} + (1 - \alpha) \cdot \gamma \cdot \Delta x_{1,j,kmax} + \alpha \cdot \gamma \cdot \Delta x_{imax,j,kmax} \quad (8)$$

$$D_{\alpha,\beta,\gamma}(x) = (1 - \alpha) \cdot (1 - \beta) \cdot (1 - \gamma) \cdot \Delta x_{1,1,1} + \alpha \cdot (1 - \beta) \cdot (1 - \gamma) \cdot \Delta x_{imax,1,1} + (1 - \alpha) \cdot \beta \cdot (1 - \gamma) \cdot \Delta x_{1,jmax,1} + (1 - \alpha) \cdot (1 - \beta) \cdot \gamma \cdot \Delta x_{1,1,kmax} + \alpha \cdot \beta \cdot (1 - \gamma) \cdot \Delta x_{imax,jmax,1} + \alpha \cdot (1 - \beta) \cdot \gamma \cdot \Delta x_{imax,1,kmax} + (1 - \alpha) \cdot \beta \cdot \gamma \cdot \Delta x_{1,jmax,kmax} + \alpha \cdot \beta \cdot \gamma \cdot \Delta x_{imax,jmax,kmax} \quad (9)$$

The calculation of the deformation ($\Delta y_{i,j,k}$, $\Delta z_{i,j,k}$) in the other directions (y, z) is the same as in the x-direction. While TFIs have the advantage of high computational efficiency in calculating internal mesh points, RBFs are suitable for dealing with mesh deformations at edge boundaries within the blade tip. The basic form of the RBFs is expressed as follows:

$$f(\mathbf{x}) = \sum_{k=1}^{n_b} \alpha_k \beta(\|\mathbf{x} - \mathbf{x}_{bk}\|) \quad (10)$$

where β is a given basis function concerning the Euclidean distance, α_k is the k-th interpolation basis of the interpolation weight coefficients, \mathbf{x}_{bk} is the position vector of the object surface nodes directly related to the motion, and n_b represents the number of boundary nodes.

To ensure the quality of the deformed mesh, two issues need to be carefully considered: 1) the size of the tip clearance is generally small, and it is very easy for the deformed mesh to intrude into the blade substrate; and 2) the mesh layers in the tip clearance are dense, the distance between layers is small, and it is very easy for the mesh lines to cross when operating the mesh deformation. Therefore, two limiting parameters are introduced: the influence region A_{region} and the attenuation rate A_{rate} .

$$Deformation_{(i,j,k)} = (\Delta x_{i,j,k}, \Delta y_{i,j,k}, \Delta z_{i,j,k}) \quad \text{if } D_{(i,j,k)_casing} < A_{region} = \text{tip size} \quad (11)$$

$$Deformation_{(i,j,k)} = (0,0,0) \quad \text{if } D_{(i,j,k)_casing} \geq A_{region} = \text{tip size} \quad (12)$$

where $Deformation_{(i,j,k)}$ represents the deformation of any grid point and $D_{(i,j,k)_shroud}$ represents the distance from any grid point to the casing. Eq. 11 and Eq. 12 can be used to ensure that the blade tip is not intruded due to grid deformation.

The grid points within A_{region} are based on the "far small, near large" mesh deformation principle. The closer the mesh point is to the deformation location of the boundary, the larger the mesh deformation is. Additionally, the farther the point is, the smaller the mesh deformation is. The attenuation rate A_{rate} of mesh deformation is proportional to the distance between the point and the specified deformation boundary. By

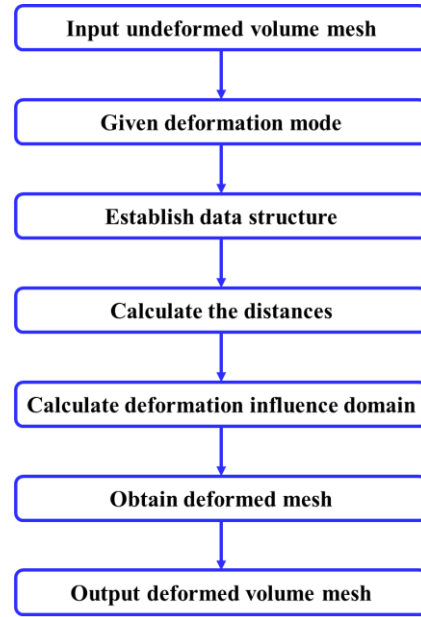


Fig. 2 Algorithm flowchart of the FMM method

determining the limiting parameters (A_{region} and A_{rate}) before conducting mesh deformation, the FMM can be used to realize the mesh movements caused by the deformation of the specified surface without changing the basic connection relationship of the original mesh points. In addition, the FMM is integrated into the in-house code HGAE to carry out numerical simulations of the flow field.

Figure 2 shows the algorithm flow of the FMM method to realize mesh deformation:

1. The volume mesh of the circular computational domain is input before performing deformation.
2. Given the deformation mode, the target location is provided for mesh deformation, i.e., the elliptical casing geometry is input as the constraint surface of the original circular computational domain to be deformed.
3. The data structure of the surface to be deformed (the original circular casing) is established.
4. The distances between all the volume grid points and the constraint surface are calculated. Then, the nearest point to the constraint surface is determined.
5. The deformation influence domain is calculated according to the limiting parameters (A_{region} and A_{rate}), and the volume grid points affected by the deformation are marked.
6. The deformation displacements at the surface points are weighted to the volume grid points according to the distances between the grid points on the surface to be deformed and the constraint surface (elliptical casing), and the new mesh can be obtained by adding the deformations to the original mesh points.
7. The deformed volume mesh of the elliptic computational domain is output.

For a single-stage turbine with an elliptical casing, the stator row and the rotor row are treated slightly differently. For the stator row, the computational domain in the absolute coordinate system does not rotate during unsteady computation, and the deformed volume mesh of its elliptical computational domain is obtained by performing only one mesh deformation according to the procedure shown in Fig. 2. In the rotor row, as the rotor blades rotate, the same rotor blade does not have the same distance from the elliptical casing (clearance size) at different time steps. In the absolute coordinate system, the elliptical casing, which works as the constraint surface, remains stationary in unsteady calculations. As the rotor row rotates, the mesh near the blade tips needs to be lengthened or shortened to fit the elliptical casing (constraint surface).

Figure 3 shows the operation mechanism of the FMM on the rotor row at different time steps in the relative coordinate system. Moreover, this figure can be used to visualize the dynamic deformation of the gridlines at different circumferential positions. If the rotor row rotates in the counterclockwise direction in the absolute coordinate system, it will remain stationary in the relative coordinate system, and the casing rotates in the clockwise direction (red arrows). The radial grid lines in the volume mesh of the circular computational domain are represented by several black line segments from the hub to the casing.

Before the calculation starts (Step 0), the user provides the volume mesh with an undeformed circular calculation domain and ellipsoidal constraint surfaces (black ellipse). Once the computation starts, at Step 1, the computational domain fits the elliptical constraint surface by mesh deformation, with the grid lines at different circumferential positions elongated or shortened (red line). As the rotor blade rotates relative to the elliptical casing, at each subsequent moment (Step n), each grid line near the elliptical casing in the computational domain is dynamically lengthened and shortened to fit the elliptical constraint surface. Finally, the unsteady flow field of the turbine rotor with an elliptical casing is numerically calculated.

In summary, considering the slight deformation of the casing (usually less than 1% of the blade span), the mesh quality, especially for boundary layers, is guaranteed during the mesh deformation procedure. The traditional method of splitting the computational domain may take tens of minutes for complex geometries to propagate through the mesh generation process prior to numerical simulation, while the FMM method does not need to regenerate the mesh of the elliptical computational domain by employing other software. Additionally, it only needs to control the movement of the mesh nodes on the original grids at each moment in the unsteady computation, which greatly improves pre-processing efficiency.

3. COMPUTATIONAL GRID AND CODE VERIFICATION

The CFD mesh for the turbine stage is obtained by AutoGrid5. The topology of O4H is used for the structured grid, where an O-grid is placed around the blades.

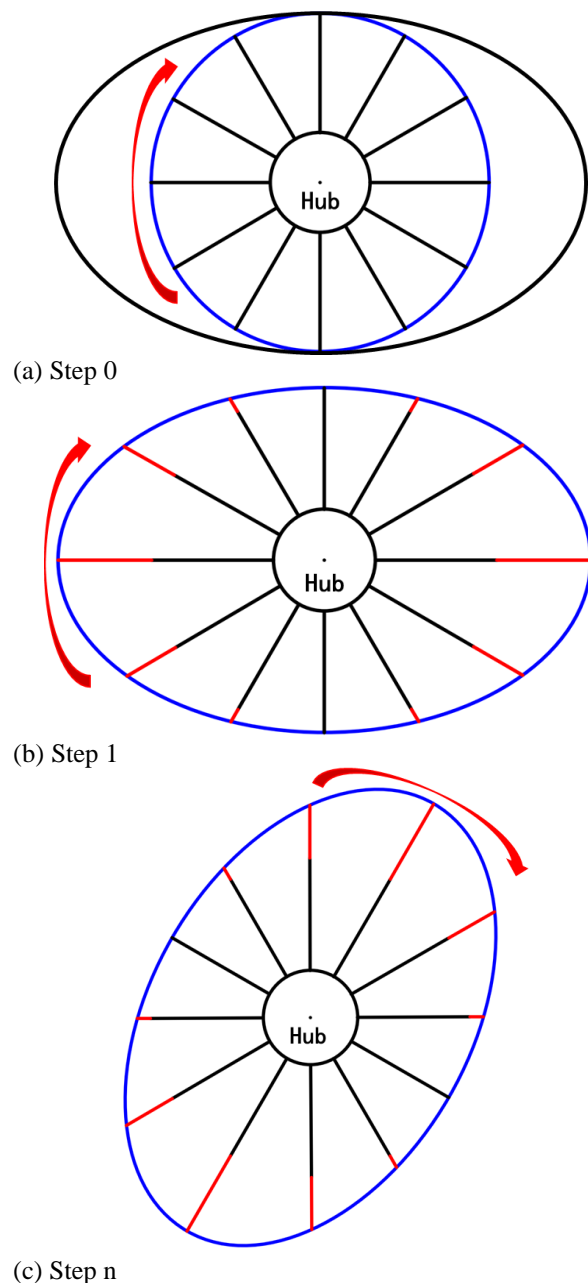


Fig. 3 Schematic diagram of the change in the calculation domain at different moments: (a) Step 0; (b) Step 1; and (c) Step n

Structured hexahedral elements are used for the turbine channels. The fluid domain of the turbine extends twice the axial chord length upstream of the stator and downstream of the rotor to establish non-reflecting boundary conditions. The total pressure and total temperature are defined as boundary conditions at the stator inlet, as shown in Table 2. At the rotor exit, the static pressure at the hub is defined under radial pressure equilibrium. In the single-passage calculation, periodic boundary conditions are defined for the stator and rotor domains. Six different mesh configurations (454 k, 612 k, 750 k, 900 k, 1063 k, and 1293 k) are used to perform grid independence verification under the same boundary conditions (Table 2).

The six mesh configurations (Level 1-6) are evaluated in terms of static pressure distribution on blade

Table 2 Boundary conditions

Parameter	Value
Inlet total temperature [K]	432.2
Inlet total pressure [KPa]	350.0
Outlet static pressure [KPa]	100.0
Rotational speed [rpm]	11000.0

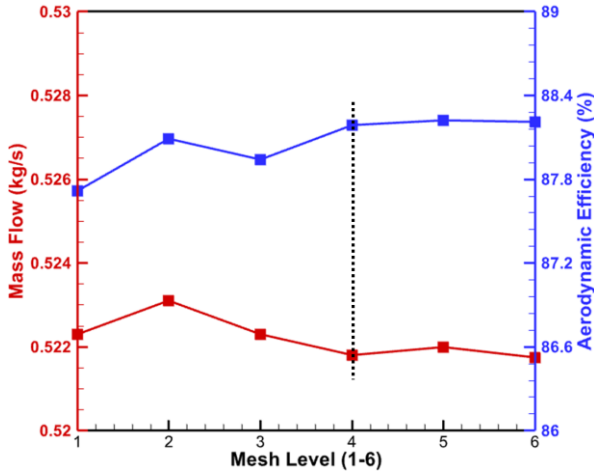


Fig. 4 Schematic diagram of grid independence verification

surfaces, exit flow angle, aerodynamic efficiency, and mass flow, respectively. Considering the page limitation, only the comparative results of aerodynamic efficiency and mass flow rate are shown (Fig. 4). The performance parameters vary significantly from level 1 to level 4, while the variation amount between level 4 and level 6 is very little. The independent verification of the number of layers at the tip clearance is also carried out, including 13, 17, and 21 grid points.

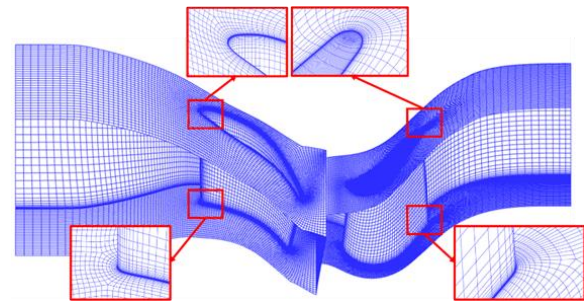
Considering the accuracy and computational cost, Level 4 configuration is selected for the subsequent study. This grid configuration has 900,434 grid points in the single-passage turbine stage, where the stator row and rotor row are distributed with $65 \times 57 \times 35$ and $93 \times 73 \times 51$ grid points in the streamwise, spanwise, and pitchwise directions, respectively. The full annular mesh is obtained by rotational duplication of the single passage mesh, with a total of more than 27.7 million mesh points. There are 17 grid points in the rotor tip clearance. The thickness of the first near-wall cell is 0.001 mm and $y^+ < 1$. The grids for single-passage and full-annulus are shown in Fig. 5.

The aerodynamic efficiencies and expansion ratios obtained from HGAE are compared with the results from commercial software (NUMECA), as shown in Table 3. The aerodynamic efficiency is defined as follows:

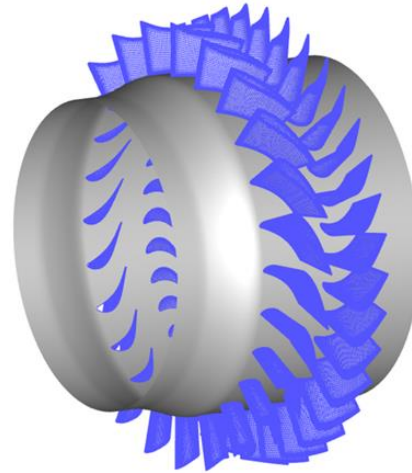
$$\eta = \frac{h_{t\ in} - h_{t\ out}}{h_{t\ in} - h_{t\ is\ out}} \quad (13)$$

where $h_{t\ in}$ represents the inlet total enthalpy, $h_{t\ out}$ represents the outlet total enthalpy, and $h_{t\ is\ out}$ is the isentropic total enthalpy in the outlet.

The difference in aerodynamic performance obtained from the different codes is less than 0.5%, and the results obtained from HGAE are in good agreement with those obtained from NUMECA.



(a)



(b)

Fig. 5 Numerical meshed model of the turbine stage: (a) single-passage stage and (b) full-annulus stage

Table 3 Comparison of the calculated aerodynamic performance

Parameter	Aerodynamic Efficiency (%)	Expansion Ratio
HGAE	88.11	3.060
NUMECA	88.53	3.061
Error	0.47%	0.03%

4. CASE STUDY

5.1 FMM Method Verification

To ensure the accuracy of the numerical calculations of the single-stage turbine for the elliptical casing, the FMM method is first validated. Fig. 6 shows a schematic diagram of the elliptical casing for the verification case. The grey area represents the blades, and the solid line (black) is the original circular casing. The external dotted line (black) is the elliptical casing, which causes the non-uniformity of the tip clearance in the circumferential direction. For the verification case (Fig. 6), the maximum clearance C_{Max} and minimum clearance C_{Min} are dimensioned at 1.96% and 1.4% of the blade height, respectively, where C_{Min} is selected as the design tip size (Table 1).

Figure 7 shows a comparison of the mesh point distributions in the blade tip before and after running the

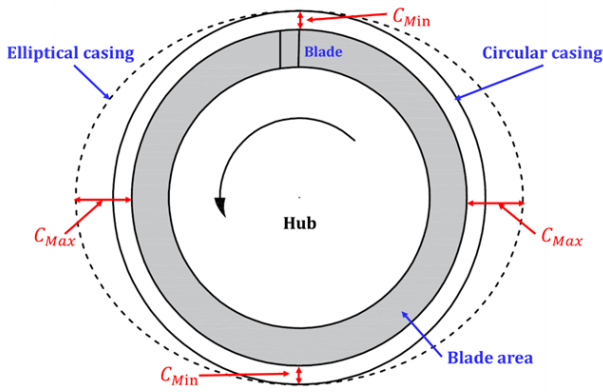


Fig. 6 The elliptical casing diagram for the verification case

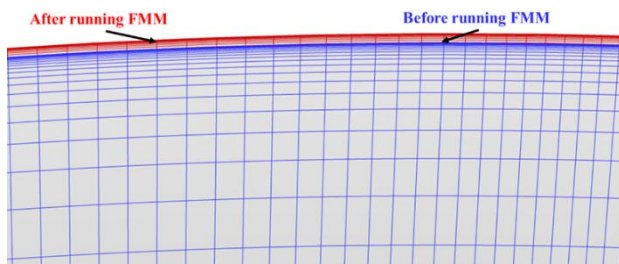


Fig. 7 Comparison of the mesh distributions within the tip clearance before and after running the FMM

FMM. Compared with the original mesh with a circular casing, the mesh topology of the elliptical computational domain does not change, giving rise to better smoothness and mesh quality. Therefore, the FMM method can generate high-quality deformation meshes for the computational domain with an elliptical casing.

4.2 Elliptical Casing Case

To determine the physical mechanism of the changes in the aerodynamic performance caused by CNTCs, two elliptical casing cases with CNTCs are investigated, identified as CNTC_1 and CNTC_2. The elliptical casing in CNTC_1 is consistent with that in the verification case (Fig. 6). The maximum (C_{Max}) and minimum clearances (C_{Min}) of CNTC_2 are 1.64% and 0.98%, respectively, of the blade height, while the circumference of the elliptical casing in this case remains the same as the circumference of the circular casing. The variations in the tip sizes for the two elliptical casing cases are typical, and the maximum absolute value of the difference between the maximum and minimum tip sizes is 0.47 mm, which satisfies the deformation range from 0.3 to 0.91 mm in previous literature (Gaffin, 1979; Hu et al., 2018; Melcher & Kypuros, 2003).

Three circular casings with different uniform tip clearances (TCs) are studied as comparative cases and are identified as TC_1.4, TC_1.68, and TC_1.96. The circular and elliptical casing cases are designed to match certain geometric commonalities for comparison, and the tip sizes for all the cases are shown in Table 4. Figure 8 shows a comparison of the circumferential tip sizes for different cases.

Table 4 Calculation case

Case	Tip size/rotor blade height [%]		
	C_{Min}	C_{Max}	C_{Ave}
TC_1.4	1.4%	1.4%	1.4%
TC_1.68	1.68%	1.68%	1.68%
TC_1.96	1.96%	1.96%	1.96%
CNTC_1	1.4%	1.96%	1.68%
CNTC_2	0.98%	1.64%	1.31%

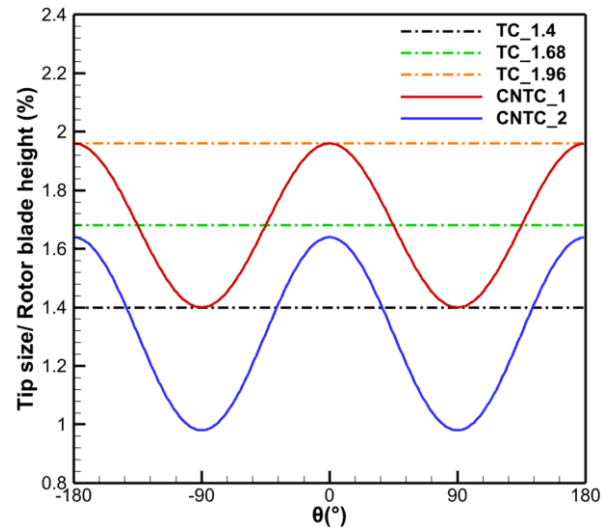


Fig. 8 Schematic of the casing for the different cases.

The minimum clearance of CNTC_1 is equivalent to that of TC_1.4, and the maximum clearance is consistent with that of TC_1.96 (1.4% and 1.96% of the rotor blade height, respectively). The average clearance of CNTC_1 and the tip size of TC_1.68 are both 1.68% of the blade height. In all the cases, the CNTC is only present circumferentially, and the tip clearance is distributed in the same way at each axial position. In this paper, both the stator and the rotor casings are elliptical, and the generation of the volume mesh for the different elliptical blade rows has been explained above (Section 2.3). Figure 8 shows a comparison of the circumferential tip sizes for different cases.

5. RESULTS AND DISCUSSIONS

Full-annulus unsteady simulations are carried out using the in-house code HGAE. The converged solution of the full-annulus steady computation is used as the initial flow field. The time step for the unsteady computation is approximately 9.469697×10^{-6} s. It takes 24 time steps for the rotor to rotate through one stator pitch, and 576 physical time steps per revolution provided sufficient temporal resolution for the flow field. Starting from approximately 500 time steps (less than one revolution), the main performance parameters (inlet and outlet flow, power, aerodynamic efficiency, expansion ratio, etc.) exhibit significant temporal periodicity. The total number of iteration steps is 2304, corresponding to approximately 4 rotor revolutions.

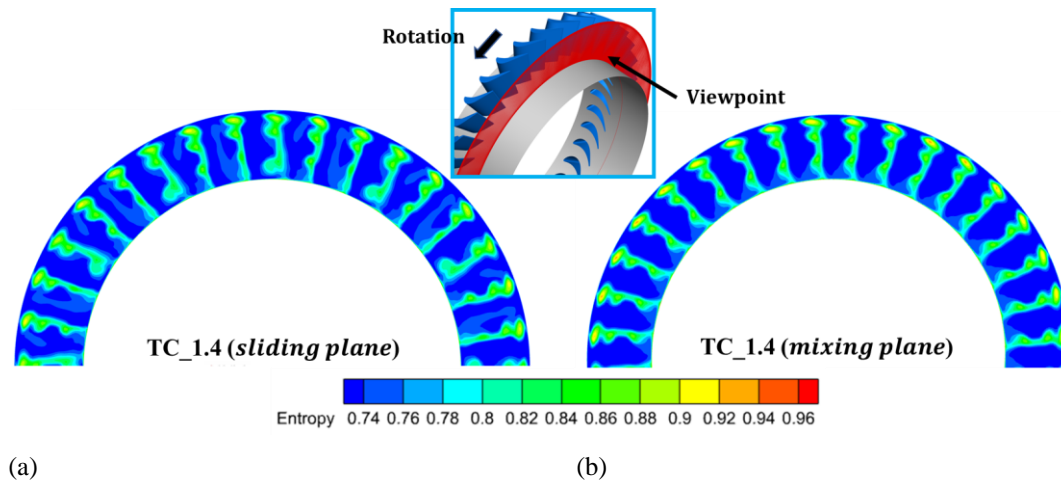


Fig. 9 Flow field at the rotor exit with different interfaces

The interface is essential for transferring data between rotating and stationary rows. Sliding planes allow the efficient transfer of the flow field data between adjacent blade rows, where the rotor row is subjected to the combined effects of wake waves, shock waves, and secondary flow from the stator row. The unsteady simulation results (Zheng et al., 2020) using the sliding plane are complicated, and it is difficult to analyse the detailed flow field. The flow field of the rotor row becomes very complex, as shown in Fig. 9a. In addition to the flow characteristics of the rotor row (rotor blade wake, passage vortex, leakage vortex, etc.) and the stator row interference (stator wake, etc.), stator-rotor interference can also be observed at the rotor row exit. Examining the variation pattern of flow characteristics with CNTCs is the key to revealing the influence of CNTCs on the aerodynamic performance and flow field. However, the flow field influenced by multiple flow characteristics is not conducive to analysing the role of different influencing factors.

To analyse the contribution of different flow characteristics in the turbine stage (stator row interference and secondary flow of rotor row, etc.) to the aerodynamic performance, step-by-step analysis of the flow characteristics of a single rotor row to the interference characteristics of the single-stage blade row is the optimal path for solving complex problems. Mixing planes can effectively shield the rotor row from the interfering effects of the stator row, and only flow features such as tip leakage vortices and passage vortices associated with the rotor row can be observed at the rotor exit (Fig. 9b), which facilitates a separate analysis of the influence mechanism of the CNTC on the flow field of the rotor row. Therefore, in this paper (Section 5.1), the aerodynamic performance and flow field of a turbine stage with CNTCs is first analysed without consideration of the stator row interference (mixing surface), followed (Section 5.2) by a discussion of the numerical simulation results considering stator row interference (sliding surface).

5.1 Aerodynamic Performance Analysis of CNTCs

The aerodynamic efficiency (Equation 1) is an important parameter for assessing the aerodynamic

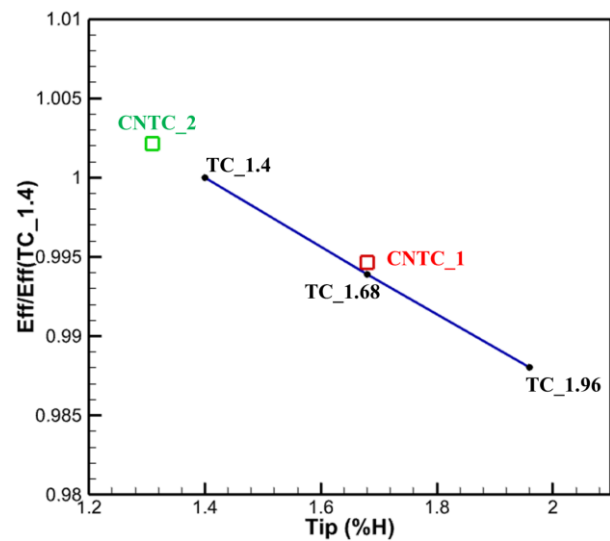


Fig. 10 Comparison of the aerodynamic efficiency for different cases

performance of a turbine stage. Figure 10 shows the aerodynamic efficiency of the turbine stage for different cases. The results for each case are expressed as changes in the aerodynamic efficiency of the design clearance (TC_1.4). The horizontal coordinate then represents the ratio of the average tip size to the blade height. The cases with circular casings (TC_1.4, 1.68, and 1.96) are represented as solid black dots in Fig. 9 and linked by blue lines. The aerodynamic efficiency varies approximately linearly with the tip clearance size. The data indicate an approximately 1.196% change in aerodynamic efficiency for a 0.56% blade height change in tip clearance, and this ratio is similar to that in the previous literature (Bunker, 2006) on flat blade tips.

The aerodynamic efficiency of the turbine stage with CNTCs is also represented in Fig. 10. The aerodynamic efficiency of CNTC_1 (red box) is reduced by 0.538% compared with that of TC_1.4, which is not ignored in engineering. However, compared with that of TC_1.4, the aerodynamic efficiency of CNTC_2 (green box) is improved by 0.212%. Significantly, the aerodynamic

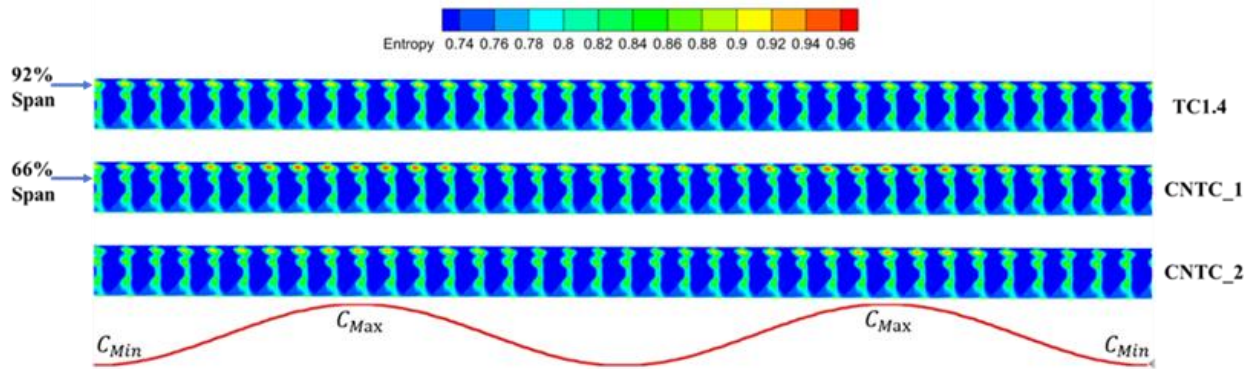


Fig. 11 Circumferential distribution of the entropy variation at the rotor exit

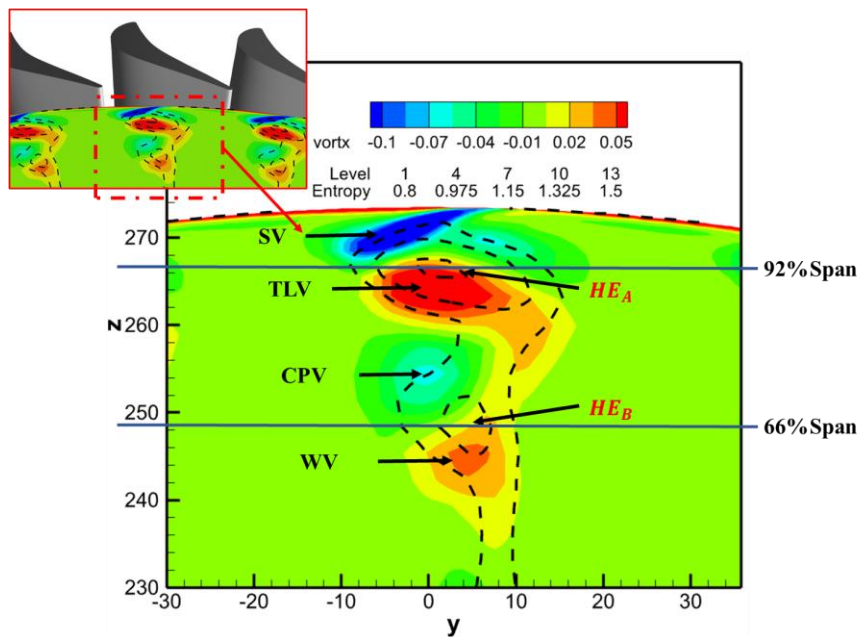


Fig. 12 Entropy and axial vorticity distributions at the rotor exit for TC_1.4

efficiencies of CNTC_1 and TC_1.68 are similar, differing by only 0.074%. Interestingly, the average clearance is the same in both cases. Moreover, CNTC_2, which has a smaller average clearance, also has the highest aerodynamic efficiency. Therefore, in the current tip size range, the average clearance may be used to evaluate the aerodynamic performance of the turbine stage. The average clearance is also mentioned as a key parameter for assessing aerodynamic performance in the tip size range studied in previous literature (DeShong et al., 2022). To understand whether the average clearance is still applicable for assessing aerodynamic efficiency in a wider range of tip sizes, it is necessary to investigate the physical mechanisms that affect aerodynamic efficiency from the perspective of flow physics.

The entropy variation is a highly suitable parameter for evaluating aerodynamic loss, and the circumferential distribution of the entropy variation at the rotor exit (Fig. 11) can be used to identify the main spanwise spans that lead to changes in aerodynamic efficiency. The entropy variation (dimensionless) is defined as follows:

$$\Delta S = \frac{P}{\rho^\gamma} \quad (14)$$

where P is the dimensionless pressure, ρ is the dimensionless density and γ is the heat capacity ratio.

For TC_1.4, the high-loss regions exhibit an alternating spatial distribution in the circumferential direction, and the number of high-loss regions corresponds to the number of rotor blades. There is no significant difference in the entropy distribution in the regions below 50% span in any of the three cases (TC_1.4, CNTC_1, and CNTC_2). Compared with that of TC_1.4, the local entropy changes significantly only at 66% and 92% spans for CNTC_1 and CNTC_2, respectively. The Secondary flow is the main flow phenomenon at these spans, and understanding the distribution characteristics of the secondary flow at the turbine exit helps to analyse the differences in aerodynamic loss for different elliptical casing cases.

Entropy variation together with vorticity diagrams can also be very good for visualizing secondary flows. The tip leakage vortex (TLV) and casing passage vortex (CPV) are the main secondary flows in the flow field on the upper part of the turbine rotor row (Fig. 12). Additionally, the tip leakage jet and the opposite flow dragged by the stationary casing create a scraping vortex (SV) on the left side of the

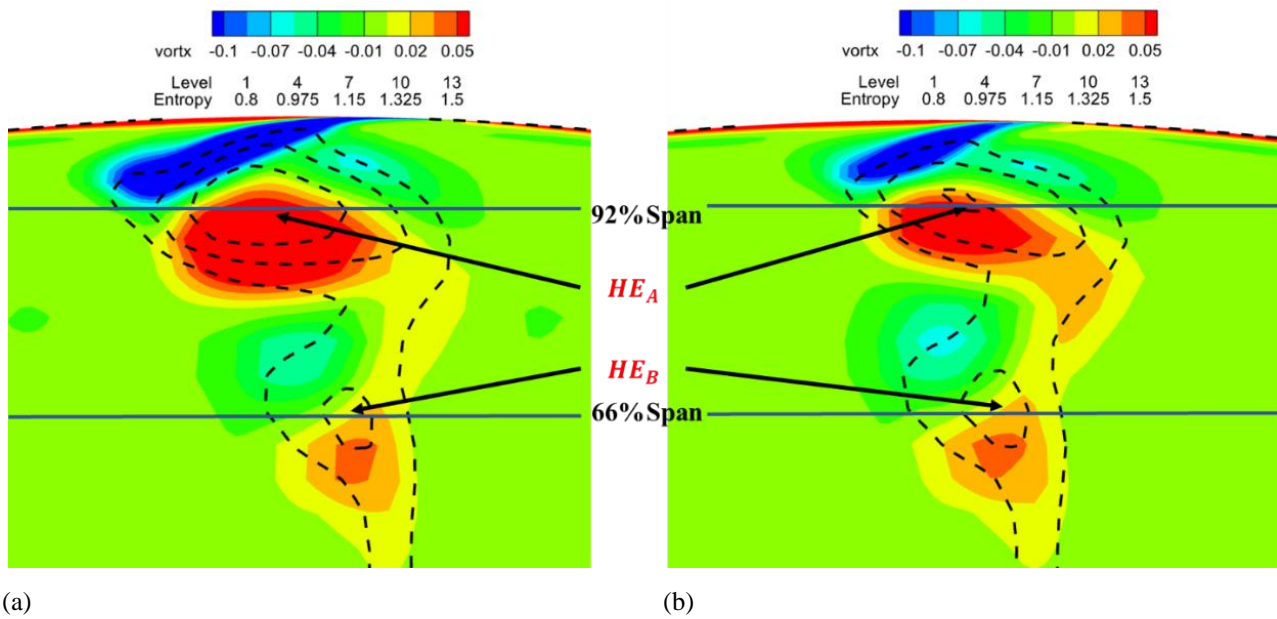


Fig. 13 Entropy and axial vorticity distributions at the rotor exit for CNTC_1: (a) rotor passage corresponding to the largest tip size and (b) rotor passage corresponding to the smallest tip size

TLV due to the relative motion of the casing and the rotor. A counterrotating wall vortex (WV) is also generated between the CPV and the wall surface.

The secondary flows mentioned above can all be identified by the contour diagram of axial vorticity in Fig. 12, where the red regions represent positive vorticity, corresponding to TLV and WV, and the regions of negative axial vorticity in blue represent SV and CPV. The two kinds of secondary flows with positive or negative vorticity represent their different spinning directions. The TLV is significantly stronger than the other secondary flows, demonstrating the importance of the TLV to the turbine stage flow field and aerodynamic performance. The black dashed line in Fig. 12 represents the entropy contour, which is presented as two high-loss regions (HE_A and HE_B). Both high-loss regions are composed of aerodynamic loss due to two pairs of secondary flows, where the losses in the HE_A region are caused mainly by TLV and SV and the main sources of loss in the HE_B region are CPV and WV. Additionally, the two high-loss regions HE_A and HE_B correspond to the alternately distributed high-entropy regions in Fig. 11.

In addition, CNTC_1 and CNTC_2 (Fig. 11) also exhibit alternating distributions of high-entropy and low-entropy regions for 2 periods at 66% and 92% spans, respectively, in addition to a high-loss region corresponding to the number of rotor blades. By comparing the circumferential distribution of the tip size (red line in the lower part of Fig. 12), the circumferential positions of the high- and low-entropy regions in the case with an elliptical casing are closely related to the tip size. To understand the aerodynamic loss due to the secondary flow at the maximum (C_{Max}) and minimum (C_{Min}) tip sizes, the exit entropy and vorticity diagrams of CNTC_1 are chosen, as shown in Fig. 13.

At the circumferential position of the maximum tip size (Fig. 13a), the influence range of the TLV increases

compared with that of TC_1.4. The development of SV near the casing, which is opposite to the rotation direction of the TLV, is promoted, and the vortex scale is significantly enhanced. Furthermore, the effect of the TLV on the PV is clear. The enhanced TLV scale removes a large amount of fluid from the periphery of the CPV, the core of the CPV is squeezed by the TLV and moves downwards, and the loss in the HE_B region, which is co-dominated by the CPV and WV, is significantly reduced. At the circumferential position of the minimum tip size (Fig. 13b), the loss in the HE_A region dominated by the TLV and SV significantly decreases. Furthermore, the flow features at the circumferential locations of the largest and smallest tip sizes for CNTC_1 are similar to those for TC_1.68 and TC_1.96, respectively. This indicates that the flow field at extreme sizes varies nearly linearly after the casing is out of roundness, and the flow features are close to those of the circular casing cases with corresponding sizes. This also explains why the average tip size can be used to assess the aerodynamic efficiency of a turbine stage with CNTCs from a flow physics perspective.

In summary, the increased TLV scale suppresses the CPV as the local tip size increases within the current tip size range, which results in increased aerodynamic loss in the HE_A region and reduced aerodynamic loss in the HE_B region. The change in total aerodynamic losses for different regions can be quantified to predict the degradation in the total aerodynamic efficiency in the turbine stage. The entropy profiles for the different cases at 66% and 92% spans are intercepted for comparison, as shown in Fig. 14. The angle in the horizontal coordinate can be used to represent the circumferential position, and the entropy profiles for different circumferential positions in the two cases are expressed in vertical coordinates as the change rate of the entropy relative to that of TC_1.4 (black line).

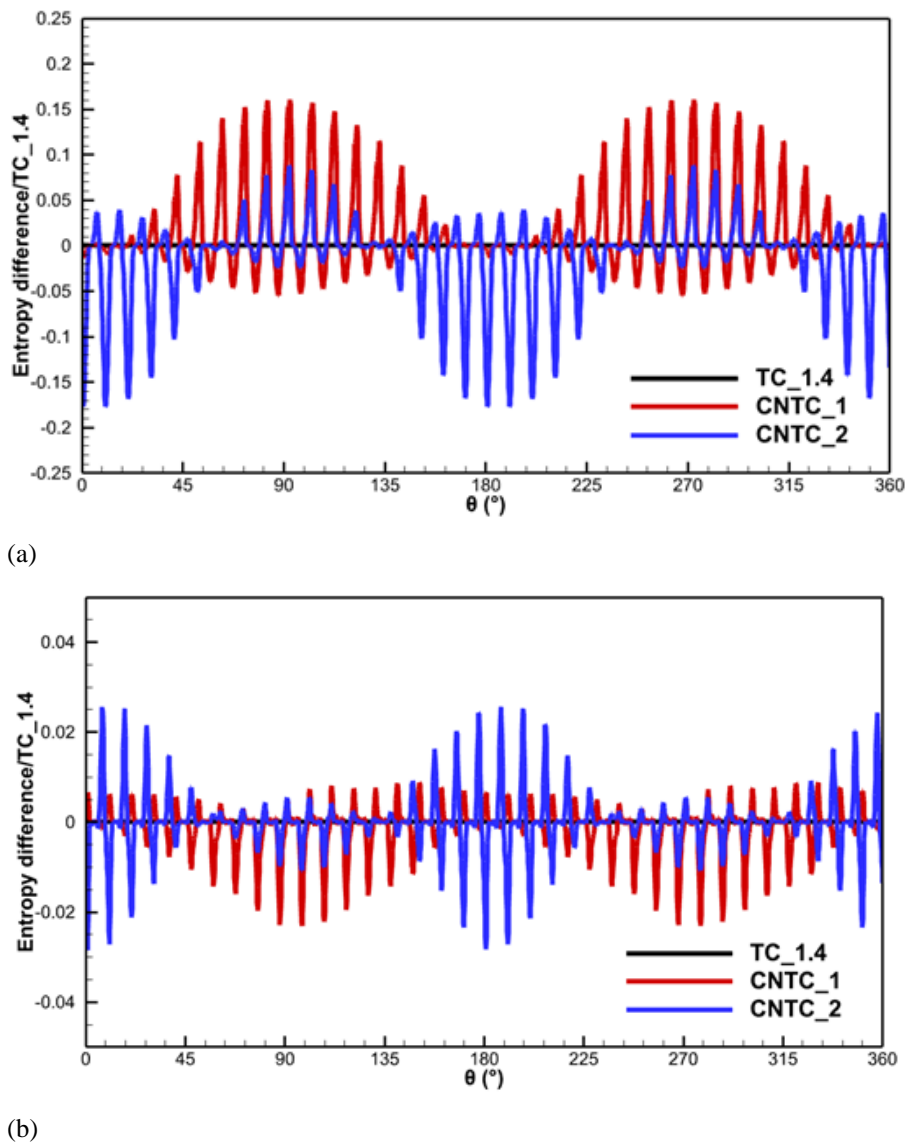


Fig. 14 The entropy profile at different circumferential positions for the different cases: (a) 92% span in the HE_A region and (b) 66% span in the HE_B region

For CNTC_1 (red line), when the rotor passes through the maximum tip size (90° and 270°), there is a maximum increase of 15.7% in the aerodynamic loss in the HE_A region (92% span) dominated by SV and TLV compared with that of TC_1.4 (black line in Fig. 14a). Moreover, the local aerodynamic loss in the HE_B region (66% span) dominated by the CPV and WV is maximally reduced by 2.3% due to the suppression of the TLV. As the rotor passes through the smallest tip size (0° and 180°), the local aerodynamic loss remains essentially constant, as the smallest tip size of CNTC_1 is the same as the tip size of TC_1.4. Therefore, the increase in the local tip size in CNTC_1 results in a much greater increase in the local aerodynamic loss at 92% span than at 66% span, preliminarily explaining the significant reduction in aerodynamic efficiency after casing ovalization (CNTC_1). The results for CNTC_2 (blue line) are different. For the HE_A region dominated by SV and TLV (92% span), the increase in the local aerodynamic loss at 90° and 270° (the maximum tip size) is much smaller than the decrease in local aerodynamic loss at 0° and 180° (the minimum tip size). Moreover, the aerodynamic loss at the

circumferential position is also reduced in the HE_B region dominated by the CPV and WV (66% span). This suggests that as the average clearance of CNTC_2 decreases, the aerodynamic loss caused by SV and TLV decreases. Although the increase in the TLV scale due to the locally increased tip size suppresses the influence range of the CPV (loss decrease), the CPV scale does not increase significantly with a decreasing local tip size, and the interaction between the secondary flows is weakened. These factors are the reasons for the increase in the aerodynamic efficiency of CNTC_2. Consequently, CNTC_1 and CNTC_2, which have different types of casing deformations, contribute negatively and positively to the aerodynamic efficiency of the turbine stage, respectively. This inconsistency is caused by the combined effect of multiple secondary flow losses (SV, TLV, and CPV) at different spans for different tip sizes. However, in previous studies that investigated turbine aerodynamic performance with elliptical casings, only the variation in the TLV scale with tip size has been analysed (Zheng et al., 2020; DeShong et al., 2022).

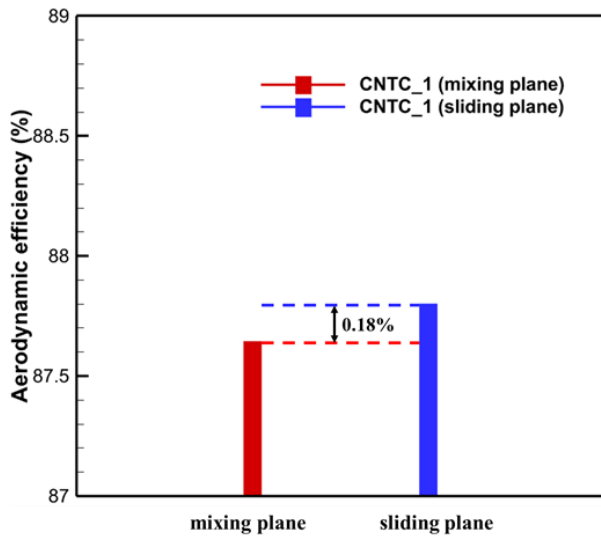


Fig. 15 Comparison of the aerodynamic efficiency for CNTC_1 with mixed and sliding surfaces

5.2 Preliminary Analysis Considering Stator Row Interference

The analyses presented above are all carried out based on calculations where the interface is a mixing plane and the effect of stator row interference is not considered. In this section, full-annular unsteady calculations are performed by using sliding planes, which are more relevant to engineering. The effect of stator row interference on the aerodynamic performance of the turbine stage with an elliptical casing is also assessed. A comparison of the aerodynamic efficiency of CNTC_1 with that of the mixed (red) and sliding (blue) planes is shown in Fig. 15.

The aerodynamic efficiency of CNTC_1 with the sliding plane is improved by 0.18% compared with that of CNTC_1 with the mixing plane. However, the aerodynamic efficiency of CNTC_1 is still significantly lower (by 0.34%) than that of TC_1.4 (Fig. 10). The elliptical casing has a significant effect on the aerodynamic loss of the secondary flow in the rotor row. However, the stator row interference weakens its influence level when considering the multi-row interaction. Since the flow analyses in the previous literature (Zheng et al., 2020; DeShong et al., 2022) focused only on the TLVs of the rotor rows, the conclusions obtained from these analyses are insufficient. Even the evaluation of performance changes may be overly pessimistic in some cases.

To understand the distribution characteristics of the aerodynamic losses considering stator row interference, the entropy profiles for the 66% and 92% spans at the rotor row exit are compared, as shown in Fig. 16.

For the HE_A region dominated by TLV and SV (Fig. 16a), the increase in entropy in these two cases is characterized in the circumferential direction by the distribution of 2 and 36 periods, which corresponds to the circumferential distribution of tip sizes and the number of rotor blades, respectively. Compared with the case where

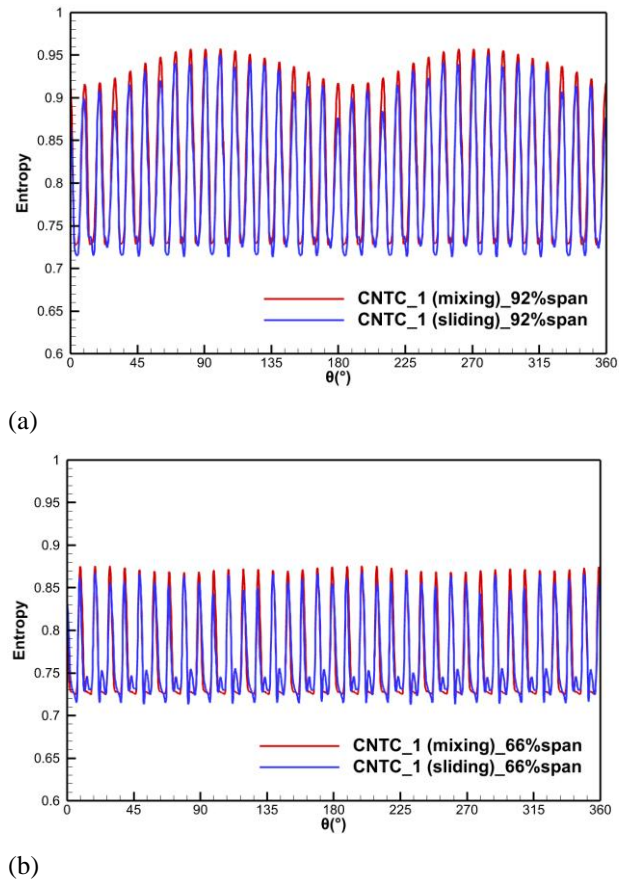


Fig. 16 The entropy profile at the rotor row exit: (a) 92% span in the HE_A region and (b) 66% span in the HE_B region

the interface is set as the mixing plane (red line in Fig. 16a), the stator row interference (blue line) weakens the loss level of the TLV and SV, and the aerodynamic loss is significantly reduced at all locations in the circumferential direction.

In contrast to the results in the previous section, the reduction in the TLV and SV scales does not promote the development of CPV or WV (Fig. 16b). Moreover, when the intersection is set as a sliding plane (blue line in Fig. 16b), the loss level in the HE_B region dominated by CPV and WV is also reduced. This suggests that stator row interference has a suppressive effect on the development of all secondary flows in the upper channel flow field. In addition to the periodic features at the rotor row exit corresponding to the number of rotor blades, the flow field characteristics of the stator row may also be included for the case with the sliding plane. To quantify the level of stator row interference, a spatial fast Fourier transform is performed on the entropy profiles at 92% and 66% spans in Fig. 16, which are illustrated in Fig. 17.

When the interface is set as a mixing plane (red line in Fig. 17), there is no stator-row interference in the rotor passage, and only 2,36-period components are included in the circumferential distribution of the rotor exit entropy. Stator row interference significantly reduces the amplitude of the 36-period component in the HE_A and HE_B regions, with reductions of 7% and 18%, respectively, at 92% and 66% spans. This finding is consistent with the results in

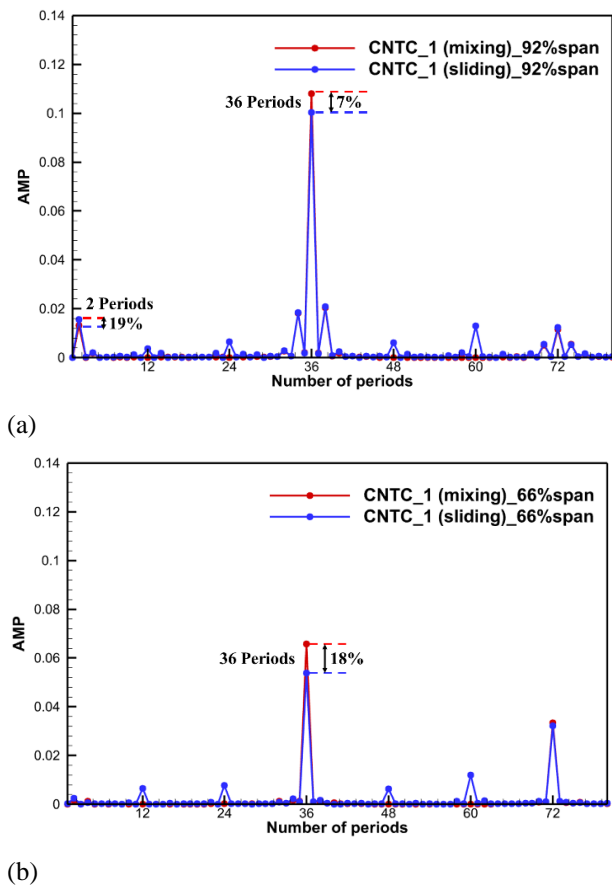


Fig. 17 Spatial fast fourier transform of the entropy profile: (a) 92% span in the HE_A region and (b) 66% span in the HE_B region

Fig. 16 and further confirms that stator row interference suppresses the development of secondary flow in the HE_A and HE_B regions. Notably, stator row interference also results in an increase (19%) in the amplitude of the component with 2 periods. It is approximately 15% of the amplitude of 36 periods (the number of rotor blades) and is also much greater than the amplitude of 24 periods (the number of stator blades), which increases the risk of low engine order (LEO) blade resonance. Whether the distribution characteristics of low periods with high amplitude introduce this kind of blade aeroelastic problem is something that needs to be focused on in future research.

6. CONCLUSION

In this paper, a new efficient fast-moving mesh method is proposed for analysing turbine aerodynamic performance with casing ovalization, which is validated using a single-stage turbine model with an elliptical casing. The results show that the FMM provides the advantages of low error, high efficiency, and easy operation compared with traditional methods that require dividing the computational domain and helps to solve elliptical casing problems quickly in scientific research or engineering applications.

A fully annular unsteady aerodynamic simulation of a transonic turbine stage with an elliptical casing was carried out using the in-house CFD code HGAE, which

integrates the FMM method. The effect of the CNTC due to casing ovalization on the flow field and aerodynamic performance was investigated. The results show that the different types of elliptical casing in CNTCs (CNTC_1 and CNTC_2) affect the aerodynamic efficiency of the turbine in a negative (decrease of 0.538%) and positive (increase of 0.212%) way, respectively. Moreover, it was innovatively concluded in this study that this difference is attributed to the interaction of multiple secondary flows (SV, TLV, and CPV) over different spans at different tip sizes. The pioneering proposal is that the factors affecting aerodynamic losses are the degree to which TLV contributes to the development of SV and the intensity at which TLV inhibits the development of CPV, not just the level of TLV mentioned in the previous literature. These findings remind engineers that they should not only pay much attention to the influence of CNTCs when applying ACC to control clearance sizes but also help to better determine the blade tip size. In addition, it was found for the first time that stator row interference can suppress the development of secondary flows in the HE_A (SV and TLV) and HE_B (CPV and WV) regions and significantly reduce aerodynamic losses at all locations in the circumferential direction. To evaluate the aerodynamic performance of the turbine stage more accurately in the future, it is necessary to consider stator row interference in CNTC studies.

Additionally, it was originally found that an elliptical casing leads to a significant increase in the aerodynamic excitation amplitude of components with 2 periods on rotor blades. Whether high-amplitude fluctuations can induce serious blade aeroelasticity problems that endanger the safe operation of aeroengines is an issue that must be addressed in future studies.

ACKNOWLEDGEMENTS

This research was funded by the National Science and Technology Major Project, China (Grant No.2017-II-0009-0023).

CONFLICT OF INTEREST

The author(s) declared no potential conflicts of interest concerning the research, authorship, and publication of this article.

AUTHORS CONTRIBUTION

All three authors have made substantial and equal contributions to this work. **Y. Zheng:** Methodology, software, validation, resources, data curation, project administration, funding acquisition. **X. B. Jin:** Validation, conceptualization, methodology, validation, formal analysis, investigation, visualization, writing—original draft preparation, writing—review and editing. **H. Yang:** Conceptualization, formal analysis, investigation, resources, supervision. All authors have read and agreed to the published version of the manuscript.

REFERENCES

- Alford, J. S. (1965). Protecting turbomachinery from self-excited rotor whirl. *Journal of Engineering for Gas Turbines and Power*, 87(4), 333–343. <https://doi.org/10.1115/1.3678270>
- Allen, C. B. (2002). Aeroelastic computations using algebraic grid motion. *The Aeronautical Journal*, 106(1064), 559-570. <https://doi.org/10.1017/S0001924000018182>
- Benito, D., Dixon, J., & Metherell, P. (2008, January). *3D thermo-mechanical modelling method to predict compressor local tip running clearances*. Turbo Expo: Power for Land, Sea, and Air. <https://doi.org/10.1115/GT2008-50780>
- Bunker, R. S. (2006). Axial turbine blade tips: function, design, and durability. *Journal of Propulsion and Power*, 22(2), 271-285. <https://doi.org/10.2514/1.11818>
- Chen, Y., Hou, A., Wang, W., & Zhang, M. (2018). Performance estimation method for nonuniform tip clearance cases. *Journal of Propulsion and Power*, 34(6), 1355-1363. <https://doi.org/10.2514/1.B36442>
- Chen, Y., Hou, A., Zhang, M., Li, J., & Zhang, S. (2015, June). *Effects of nonuniform tip clearance on fan performance and flow field*. Turbo Expo: Power for Land, Sea, and Air. <https://doi.org/10.1115/GT2015-42133>
- De Boer, A., Van der Schoot, M. S., & Bijl, H. (2007). Mesh deformation based on radial basis function interpolation. *Computers & structures*, 85(11-14), 784-795. <https://doi.org/10.1016/j.compstruc.2007.01.013>
- DeShong, E. T., Siroka, S., Berdancier, R. A., & Thole, K. A. (2022). Evaluating the influence of rotor-casing eccentricity on turbine efficiency including time-resolved flow field measurements. *Journal of Turbomachinery*, 144(2), 021012. <https://doi.org/10.1115/1.4052318>
- Erhard, J., & Gehrler, A. (2000, May). *Design and construction of a transonic test-turbine facility*. Turbo Expo: Power for Land, Sea, and Air. <https://doi.org/10.1115/2000-GT-0480>
- Göttlich, E., Neumayer, F., Woisetschläger, J., Sanz, W., & Heitmeir, F. (2004). Investigation of stator-rotor interaction in a transonic turbine stage using laser doppler velocimetry and pneumatic probes. *Journal of Turbomachinery*, 126(2), 297-305. <https://doi.org/10.1115/1.1649745>
- Gaffin, W. O. (1979). *JT9D-70/59 Improved high pressure turbine active clearance control system* (No. NASA-CR-159661). <https://ntrs.nasa.gov/api/citations/19790023037/downloads/19790023037.pdf>
- Gaitonde, A. L., & Fiddes, S. P. (1995). A three-dimensional moving mesh method for the calculation of unsteady transonic flows. *The Aeronautical Journal*, 99(984), 150-160. <https://doi.org/10.1017/S0001924000027135>
- Gaitonde, A., & Fiddes, S. (1993, January). *A moving mesh system for the calculation of unsteady flows*. 31st Aerospace Sciences Meeting. <https://doi.org/10.2514/6.1993-641>
- Hu, J. L., Gao, J. H., Liu, G., Cui, L., & Guo, B. T. (2018). Experiment of high pressure turbine case based on active clearance control system. *Journal of Propulsion Technology*, 39(4), 740-750. <https://doi.org/10.13675/j.cnki.tjjs.2018.04.003>
- Jameson, A. (1991, June). *Time dependent calculations using multigrid, with applications to unsteady flows past airfoils and wings*. 10th Computational fluid dynamics conference. <https://doi.org/10.2514/6.1991-1596>
- Jiang, C., Hu, J., Wang, J., & Cong, L. (2020). Numerical investigation on flow field distribution of eccentric compressors based on steady and unsteady cfd methods. *Energies*, 13(22), 6081. <https://doi.org/10.3390/en13226081>
- Lattime, S. B., & Steinetz, B. M. (2004). High-pressure-turbine clearance control systems: current practices and future directions. *Journal of Propulsion and Power*, 20(2), 302-311. <https://doi.org/10.2514/1.9255>
- Lavagnoli, S., De Maesschalck, C., & Andreoli, V. (2017). Design considerations for tip clearance control and measurement on a turbine rainbow rotor with multiple blade tip geometries. *Journal of Engineering for Gas Turbines and Power*, 139(4), 042603. <https://doi.org/10.1115/1.4034919>
- Liu, Y., Tan, L., & Wang, B. (2018). A review of tip clearance in propeller, pump and turbine. *Energies*, 11(9), 2202. <https://doi.org/10.3390/en11092202>
- Melcher, K. J., & Kypuros, J. A. (2003, December). *Toward a fast-response active turbine tip clearance control*. 16th International Symposium on Airbreathing Engines (No. E-14185). <https://ntrs.nasa.gov/api/citations/20040031316/downloads/20040031316.pdf>
- Menter, F. R. (1993, July). *Zonal two equation kw turbulence models for aerodynamic flows*. 23rd fluid dynamics, plasmadynamics, and lasers conference. <https://doi.org/10.2514/6.1993-2906>
- Menter, F. R. (1994). Two-equation eddy-viscosity turbulence models for engineering applications. *AIAA Journal*, 32(8), 1598-1605. <https://doi.org/10.2514/3.12149>
- Olsson, W. J., & Martin, R. L. (1982). *B747/JT9D flight loads and their effect on engine running clearances and performance deterioration; BCAC NAIL/P and WA JT9D engine diagnostics programs* (No. NAS 1.26: 165573). <https://ntrs.nasa.gov/api/citations/19820020420/downloads/19820020420.pdf>

[nloads/19820020420.pdf](#)

- Pan, Y., Yuan, Q., Huang, G., Gu, J., Li, P., & Zhu, G. (2020). Numerical investigations on the blade tip clearance excitation forces in an unshrouded turbine. *Applied Sciences*, 10(4), 1532. <https://doi.org/10.3390/app10041532>
- Reuther, J., Jameson, A., Farmer, J., Martinelli, L., & Saunders, D. (1996, January). *Aerodynamic shape optimization of complex aircraft configurations via an adjoint formulation*. 34th aerospace sciences meeting and exhibit. <https://doi.org/10.2514/6.1996-94>
- Roe, P. L. (1981). Approximate riemann solvers, parameter vectors, and difference schemes. *Journal of Computational Physics*, 43(2), 357-372. [https://doi.org/10.1016/0021-9991\(81\)90128-5](https://doi.org/10.1016/0021-9991(81)90128-5)
- Song, S. J. (1998). Inviscid rotordynamic damping forces due to nonaxisymmetric tip clearance in turbines. *AIAA Journal*, 36(12), 2163-2169. <https://doi.org/10.2514/2.340>
- Song, S. J., & Martinez-Sanchez, M. (1997a). Rotordynamic forces due to turbine tip leakage: Part I—blade scale effects. *Journal of Turbomachinery*, 119(4), 695–703. <https://doi.org/10.1115/1.2841179>
- Song, S. J., & Martinez-Sanchez, M. (1997b). Rotordynamic forces due to turbine tip leakage: Part II—radius scale effects and experimental verification. *Journal of Turbomachinery*. 119(4), 704–713. <https://doi.org/10.1115/1.2841180>
- Zhang, L. P. (2010). Reviews of moving grid generation techniques and numerical methods for unsteady flow. *Advances in Mechanics*, 40(4), 424-447. <https://doi.org/10.6052/1000-0992-2010-4-J2009-123>
- Zheng, Y. (2004). *Computational aerodynamics on unstructured meshes* [Doctoral dissertation, Durham University]. <https://etheses.dur.ac.uk/2830>
- Zheng, Y., & Yang, H. (2011). Coupled fluid-structure flutter analysis of a transonic fan. *Chinese Journal of Aeronautics*, 24(3), 258-264. [https://doi.org/10.1016/S1000-9361\(11\)60031-9](https://doi.org/10.1016/S1000-9361(11)60031-9)
- Zheng, Y., & Yang, H. (2013). Full assembly fluid/structured flutter analysis of a transonic fan. *Journal of Beijing University of Aeronautics and Astronautics*, 39(5), 626-630. <https://doi.org/10.13700/j.bh.1001-5965.2013.05.024>
- Zheng, Y., Jin, X., & Yang, H. (2022). Effects of asymmetric vane pitch on reducing low-engine-order forced response of a turbine stage. *Aerospace*, 9(11), 694. <https://doi.org/10.3390/aerospace9110694>
- Zheng, Y., Jin, X., Yang, H., Gao, Q., & Xu, K. (2020, September). *Effects of circumferential nonuniform tip clearance on flow field and performance of a transonic turbine*. Turbo Expo: Power for Land, Sea, and Air. American Society of Mechanical Engineers. <https://doi.org/10.1115/GT2020-15295>
- Zheng, Y., Wang, B., Wang, J., & Xiao, D. (2012). Mesh deforming technique based on compatibility of multi-block structured mesh deformation and its application to blade aerodynamic analysis in turbomachinery. *Aeronautical Computing Technique*, 42, 83-87. <https://doi.org/10.3969/j.issn.1671-654X.2012.01.023>